Controlled hydroxyapatite biomineralization in an ~810 million-year-old unicellular eukaryote

PALEONTOLOGY

Controlled hydroxyapatite biomineralization in an ~810 million-year-old unicellular eukaryote

Phoebe A. Cohen,[1]* Justin V. Strauss,[2] Alan D. Rooney,[3†] Mukul Sharma,[2] Nicholas Tosca[4]

Biomineralization marks one of the most significant evolutionary milestones among the Eukarya, but its roots in the fossil record remain obscure. We report crystallographic and geochemical evidence for controlled eukaryotic biomineralization in Neoproterozoic scale microfossils from the Fifteenmile Group of Yukon, Canada. High-resolution transmission electron microscopy reveals that the microfossils are constructed of a hierarchically organized interwoven network of fibrous hydroxyapatite crystals each elongated along the [001] direction, indicating biological control over microstructural crystallization. New Re-Os geochronological data from organic-rich shale directly below the fossil-bearing limestone constrain their age to <810.7 ± 6.3 million years ago. Mineralogical and geochemical variations from these sedimentary rocks indicate that dynamic global marine redox conditions, enhanced by local restriction, may have led to an increase in dissolved phosphate in pore and bottom waters of the Fifteenmile basin and facilitated the necessary geochemical conditions for the advent of calcium phosphate biomineralization.

INTRODUCTION

Eukaryotic biomineralizing organisms represent a major component of Phanerozoic diversity, and their rise to prominence forever shifted both ecological dynamics and biogeochemical cycles (*1*–*3*). Although biomineralization evolved multiple times in different eukaryotic clades, mineralized structures are not abundant in the fossil record until the terminal Ediacaran and Cambrian expansion in metazoan skeletons (*2*). Evidence of pre-Ediacaran biologically controlled mineralization has never been definitively identified. Thus, both the timing and the environmental circumstances surrounding the evolution of biologically controlled mineralization are unknown (*2*).

Apatitic scale microfossils (ASMs) from the Fifteenmile Group of Yukon, Canada, have long been thought to represent a crucial landmark in the pre-Ediacaran history of biomineralization (*4*, *5*), but their age and mineralogical origin have remained problematic. These fossils display a wide diversity of morphologies (*4*, *6*), and they are interpreted as cell coverings similar in function to those found in modern coccolithophores and other scale-forming protists, although their exact taxonomic placement within the Eukarya is still uncertain (*5*, *6*). The ASM assemblage is preserved in an approximately 60-m-thick section of lime mudstone and calcareous black and gray shale of the Fifteenmile Group near Mount Slipper in west-central Yukon, Canada (Fig. 1, fig. S1, and Materials and Methods). Previous age constraints on the fossiliferous strata ranged from ca. 811 to 717 Ma (million years ago) on the basis of regional and global Sr and C chemostratigraphic correlations (*7*) and placed the ASM assemblage between the Bitter Springs (ca. 811 Ma) and Islay (ca. 735 Ma) negative carbon isotope excursions (anomalies). Addressing this age uncertainty is critical for calibrating the earliest evidence for biomineralization and placing the fossil assemblage within the proper evolutionary and environmental context.

Although previous work showed that the ASM taxa are constructed of apatite and organic carbon (*5*), a primary origin for the ASM apatite has remained an open question. Phosphatic replacement is widespread in the Neoproterozoic and Cambrian fossil record, and existing data on the ASM taxa have not ruled out a diagenetic origin for phosphate (*8*). In addition, calcium phosphate biomineralization is rare among modern marine microeukaryotes because phosphate can be a limiting nutrient in many marine ecosystems (*9*, *10*) and the energetic cost of biomineralizing with a calcium phosphate phase in these environments would be prohibitively high (*2*, *11*). Even heterotrophs in modern pelagic marine systems can be P-limited because of limitation in their prey (*12*). Thus, it is unclear why and how phosphate biomineralization would have emerged in the Neoproterozoic.

Here, we present new high-resolution transmission electron microscopy (HR-TEM) data that reveal a primary and biologically controlled origin for ASM mineralogy and identify it as hydroxyapatite (HAP). Combining these microanalytical results with a new radiometric age constraint on the fossil assemblage establishes the ASMs as the oldest known eukaryotic representatives of biologically controlled mineralization. New geochemical and mineralogical data from the ASM-bearing strata place this Neoproterozoic HAP biomineralization event in paleoenvironmental context. These data show that phosphate biomineralization was permitted by elevated marine phosphate concentrations that were, in turn, influenced by local redox instability associated with the protracted ventilation of the Neoproterozoic oceans.

RESULTS

Mineralogy of ASMs

To determine the precise composition of the ASMs, we used HR-TEM of single specimens picked from macerates and deposited directly onto Cu grids (Fig. 2 and fig. S2). Imaging shows that ASM specimens are constructed of a systematically interwoven network of fibrous crystals (Fig. 2, D and E). The network is constructed of geometrically organized strands ~0.6 to 1.0 μm in thickness (Fig. 2, C and E, and fig. S1), which are, in turn, composed of bundles of fibrous crystals ~50 nm in width and up to 1 to 2 μm in length (Fig. 2 and fig. S2). Energy-dispersive x-ray microanalysis indicates that the fossil material is composed of P, C, O, and Ca and contains no detectable impurities (for example, F or Cl), confirming that the fossils are constructed of HAP rather than the highly substituted diagenetic carbonate fluorapatite

[1]Geosciences Department, Williams College, Williamstown, MA 01267, USA. [2]Department of Earth Sciences, Dartmouth College, Hanover, NH 03755, USA. [3]Department of Earth and Planetary Sciences, Harvard University, Cambridge, MA 02138, USA. [4]Department of Earth Sciences, University of Oxford, Oxford OX1 3AN, UK.
*Corresponding author. Email: pac3@williams.edu
†Present address: Department of Geology and Geophysics, Yale University, New Haven, CT 06511, USA.

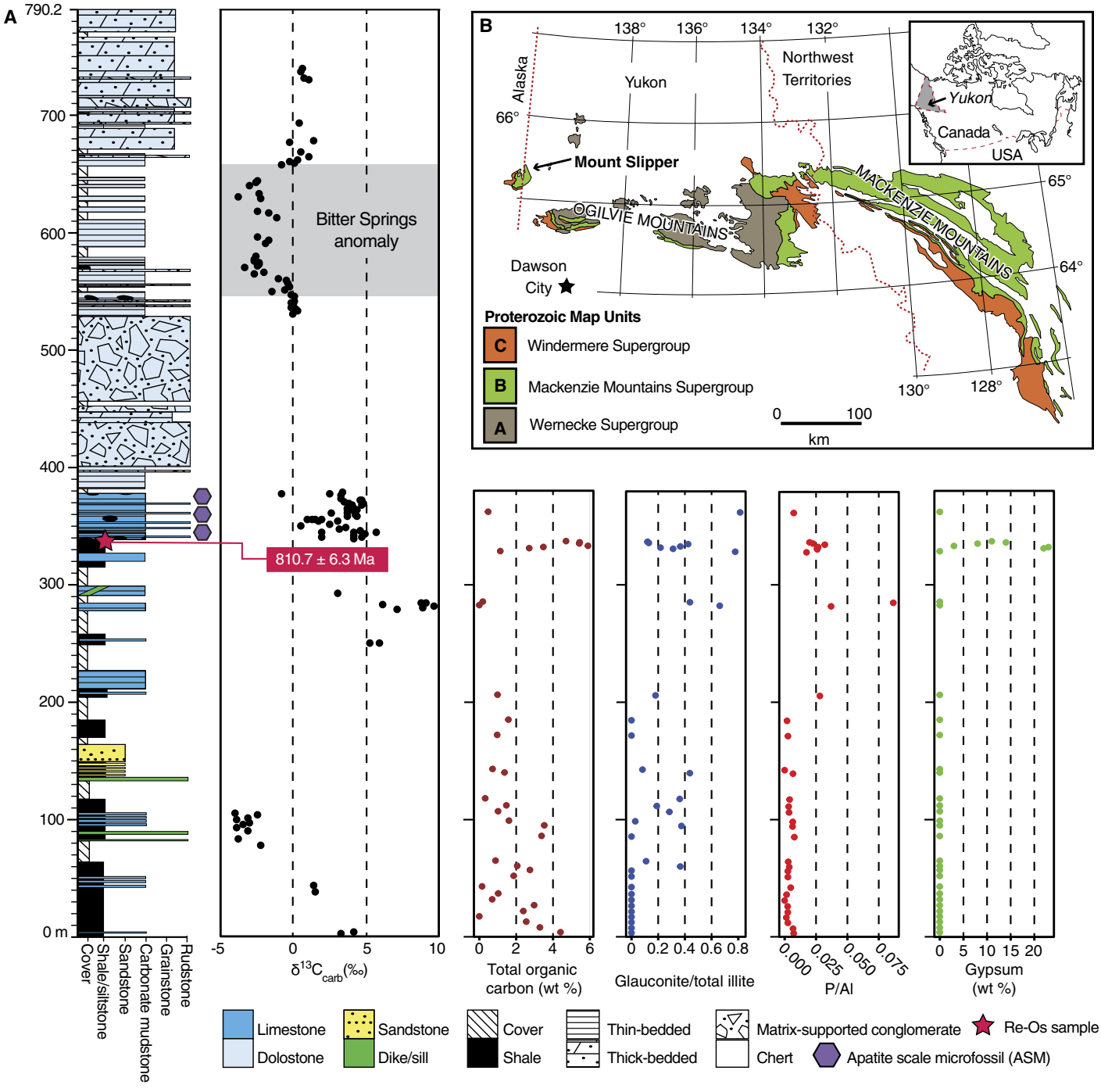

Fig. 1. Stratigraphy, geochemistry, and mineralogy of Mount Slipper strata. (**A**) Left: Composite stratigraphic column at Mount Slipper showing lithology, carbon isotope chemostratigraphy, and the location of the Re-Os horizon relative to the fossiliferous strata. Right: Data for TOC (*18*), glauconite/illite polymorphs, P/Al (*18*), and gypsum weight percent in the Mount Slipper section. Additional geochemical and mineralogical data can be found in fig. S3 and table S1. (**B**) Map of northwest Canada showing the location of Mount Slipper; inset map of Canada showing the location of Yukon. See Materials and Methods for more information on Mount Slipper sedimentology, stratigraphy, and nomenclature.

(fig. S3). Selected area electron diffraction analyses acquired throughout the specimens further indicate that the fibrous HAP crystals are everywhere elongated along the [001] direction (Fig. 2F and fig. S2E).

The primary microstructure preserved in the ASMs reflects a high degree of biological control over HAP crystallization. Morphological control over skeletal components, specifically the development of fibrous HAP elongated along [001], can only be achieved through the inhibition of selected crystal faces during growth. Although nucleation and growth in the Ca-PO_4-H_2O system take place through a variety of precursors that are metastable with respect to crystalline HAP (*13*), a commonly observed pathway in protein-mediated HAP crystallization involves the formation of amorphous calcium

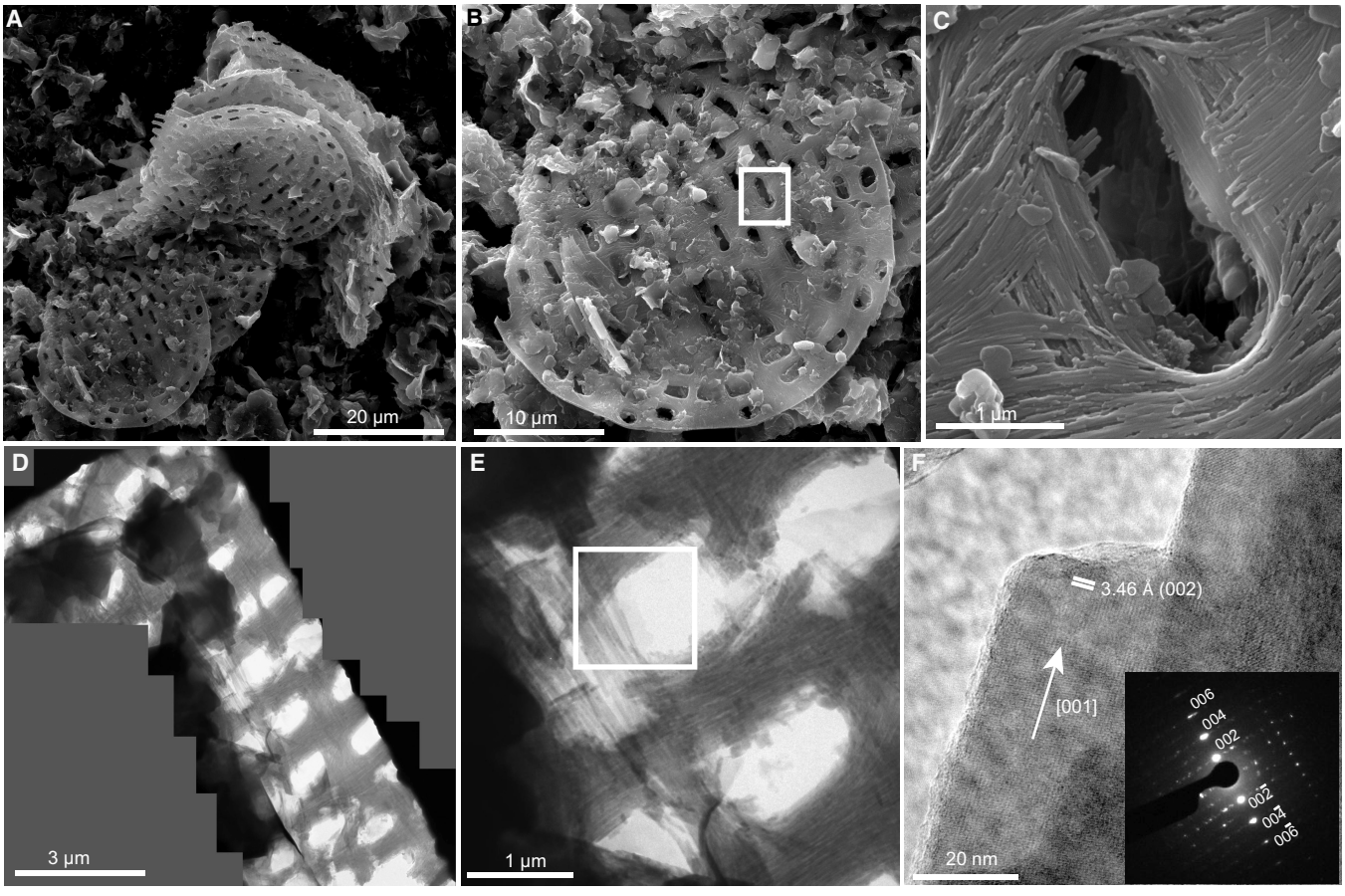

Fig. 2. Electron micrographs of an ASM specimen. (**A**) Scanning electron micrograph of a cluster of unnamed ASM taxa. (**B**) Scanning electron micrograph of a single unnamed ASM specimen from (A). (**C**) Area shown in white box in (B): Close-up of a single pore in scale surface showing HAP fibers. (**D**) Mosaic TEM image of a different ASM specimen with similar morphology to that shown in (A). Note the organization of HAP fibers into bundles that are interwoven to form a larger-scale meshwork structure with ovoid-shaped pores ~1 to 2 μm wide. (**E**) HR-TEM image of the edge of pore from (D) showing interwoven HAP fibers. (**F**) HR-TEM image of a single crystal of HAP from the white box in (E). Note that the image is rotated 45°. Spacing and direction are shown. Inset: Single area electron diffraction pattern of the crystal in fig. S2D.

phosphate and transformation to octacalcium phosphate (OCP) (*14*). Differential binding energies of protein complexes on OCP crystal faces have been shown to enhance crystal growth along [001] (*14*), and subsequent transformation from metastable OCP to HAP preserves this elongation because of structural similarities between the two phases (*13*, *14*). Therefore, protein-mediated crystal growth studies support the inference that a similar sequence of reaction steps is likely to have controlled the morphology, crystallographic orientation, and hierarchical organization of fibrous HAP crystals present in ASMs. These nonclassical crystallization pathways are common in biomineralization because they offer organisms efficient transport of skeletal precursor materials and greater control over mineral reactivity and crystallization (*15*). The preservation of consistent hierarchical organization, the persistence of HAP, and the retention of preferred crystallographic orientation indicate that ASMs were formed via a controlled eukaryotic biomineralization pathway and that their original structure was largely unmodified by diagenetic replacement or recrystallization.

Geochronological constraints on the ASM assemblage

To provide a maximum depositional age on the ASM-bearing strata and refine current chemostratigraphic age models for the Fifteenmile Group at Mount Slipper, we performed Re-Os geochronology on black, organic-rich shale from a horizon 4.15 m below the base of the fossiliferous interval (Fig. 1A). These data yield a model 1 age of 810.7 ± 5.8 Ma (6.3 Ma) [bracketed uncertainty includes the 0.35% uncertainty in the ^{187}Re decay constant, λ; n = 8; mean square of weighted deviates (MSWD), 0.47; 2σ; initial ^{187}Os/^{188}Os, 0.43 ± 0.01; Fig. 3 and table S1]. This new Re-Os age is identical, within uncertainty, to U-Pb ages on zircon from volcanic horizons beneath the Bitter Springs anomaly in both the nearby Ogilvie Mountains of Yukon and the Tambien Group of Ethiopia (*16*, *17*). Therefore, our new radiometric age constraint places the appearance of mineralized ASMs before the Bitter Springs excursion (BSE; Fig. 1) and makes these fossils one of the most well-calibrated Tonian assemblages to date.

Mineralogical and geochemical analyses from the Fifteenmile Group

To complement previous paleoredox data (*18*) and place new mineralogical constraints on the fossiliferous portion of the Fifteenmile Group, we performed high-resolution powder x-ray diffraction analyses on organic-rich black shale samples from the Mount Slipper stratigraphic section. Existing redox geochemical data from the underlying shale succession highlight prominent anoxia and intermittent euxinia within the Fifteenmile basin (*18*), with a marked increase in both K/Al and Fe/Al upsection, as well as increases in P, V,

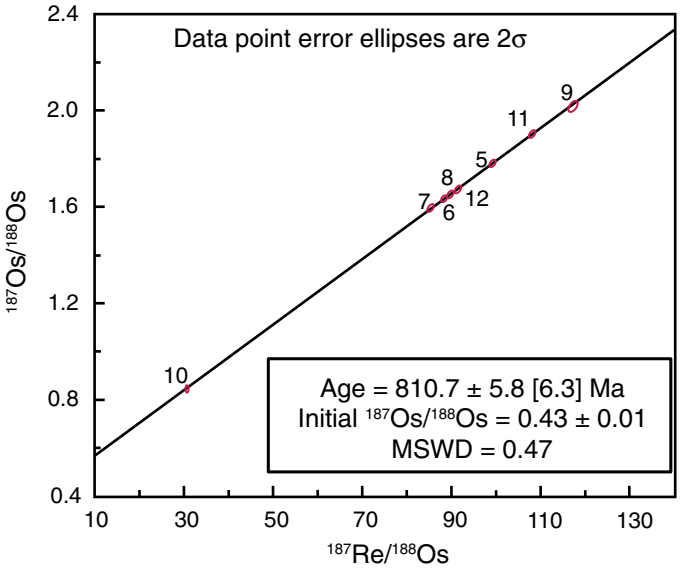

Fig. 3. Re-Os isochron diagram for Mount Slipper 1406 samples. The age uncertainty of 6.3 Ma also includes the uncertainty associated with the ^{187}Re decay constant. All isotopic composition data and elemental data can be found in table S1.

Mo, and total organic carbon (TOC) contents near the transition into the ASM-bearing strata (Fig. 1A, fig. S4, and table S1) (*18*). The new mineralogical data show that the abundance of glauconite, a redox-sensitive Fe(II)-Fe(III) authigenic silicate, and gypsum also increases relative to the other illite polymorphs' upsection (Fig. 1A, fig. S4, and table S1). This mineralogical shift is also coincident with sedimentological evidence for basinal restriction in the form of centimeter-scale carbonate-replaced gypsum precipitates (fig. S1D) and a prominent transition from siliciclastic- to carbonate-dominated strata in the Fifteenmile basin (Fig. 1A).

DISCUSSION

Geochronological implications and context

Our new age constraint and high-resolution carbon isotope chemostratigraphy from Mount Slipper place the ASM assemblage below the BSE (Fig. 1A). This result conflicts with previous interpretations that indicated that the assemblage was above the BSE (*7*, *16*). Critically, the $^{87}Sr/^{86}Sr$ data presented by Macdonald *et al.* (*7*) as a key component of their geochronological constraints are still consistent with our age model because Tonian Sr isotopic compilations [for example, see the study of Cox *et al.* (*19*)] do not show significant variability surrounding the BSE; moreover, all of the $^{87}Sr/^{86}Sr$ data presented by Macdonald *et al.* (*7*) come from unaltered fossiliferous strata that yield enriched $\delta^{13}C_{carb}$ values. Thus, Macdonald *et al.*'s (*7*) placement of the BSE at Mount Slipper was primarily influenced by the presence of depleted $\delta^{13}C_{carb}$ values within the so-called "upper shale" unit of the Fifteenmile Group. Our reexamination of these thin argillaceous limestone strata suggests that their primary $\delta^{13}C_{carb}$ values may be compromised by a lack of carbonate buffering (*20*); therefore, we reinterpret the nadir of the BSE to occur higher within the Mount Slipper succession, where we see a well-developed negative isotopic anomaly that resembles the form and magnitude of other BSEs both regionally and globally (Fig. 1A) (*16*, *17*, *21*). This is consistent with the new geochronological and chemostratigraphic data presented herein and emphasizes that although correlations based on chemostratigraphic relationships are essential in the Proterozoic, radiometric dates are required to fully elucidate the absolute and relative timing of paleontological and stratigraphic correlations.

Tectonically, climatically, and biologically, the Neoproterozoic era was one of the most eventful chapters in Earth's history. However, a lack of detailed biostratigraphy and the relative paucity of strata amenable to U-Pb radiometric dating have made the reconstruction of the timing of significant climatic and evolutionary events a major challenge. The new Re-Os age presented herein adds to the growing number of high-precision Neoproterozoic Re-Os and U-Pb ages (*16*, *17*, *22*–*25*), which, together, provide a new temporal framework to more fully elucidate the relationship between biotic and abiotic events (*26*). Specifically, this age greatly refines existing biostratigraphic and chemostratigraphic correlations with globally distributed Tonian strata, allows for more focused work on the spatial and temporal distribution of the ASMs, and firmly places the fossil record of ASM biomineralization in the context of evolving Neoproterozoic oceans.

The ASM assemblage arose during a critical interval of the Neoproterozoic. In addition to marked increases in eukaryotic diversity (*26*, *27*), molecular clocks indicate that the early to mid-Neoproterozoic may have witnessed the emergence of the earliest metazoans (*28*). Coincident with this, Tonian seawater appears to reflect a prominent state of geochemical transition (*29*–*31*). On the one hand, global geochemical data sets record dominantly anoxic bottom waters (*30*), yet the first significant sulfate evaporite deposits testify to the growth and deposition of an oxidized sulfur reservoir (*29*). At the same time, marine shale compilations indicate enhanced P deposition from Tonian-Cryogenian basins as compared to earlier time intervals (*32*), which may partly reflect enhanced P delivery through the weathering of rift-related volcanics (*19*, *33*) associated with the incipient breakup of Rodinia (*34*). Together, the juxtaposition of tectonic, environmental, and biological factors in the early to mid-Neoproterozoic may have set the stage for phosphate biomineralization in eukaryotic taxa.

Conditions at Mount Slipper

Set in this context, mineralogical and geochemical data from Mount Slipper provide new insight into the mechanisms that would have made P more available to biomineralizing organisms. The increase in glauconite abundance observed at Mount Slipper (Fig. 1) indicates that bottom and pore water paleoredox conditions most likely fluctuated between anoxic and oxic conditions as the Fifteenmile basin became more restricted. At the same time, a dominantly anoxic and ferruginous Fe speciation signal implies that dissolved oxygen must have appeared infrequently during the time-integrated diffusional contact between sediments and overlying bottom water (*35*). Local redox fluctuations would have promoted the rapid bacterial recycling of phosphorus at the sediment–pore water interface, similar to modern semirestricted basins that experience variable redox conditions (*36*). Although this phosphorus was likely concentrated in pore and bottom waters, modern analogs indicate that it would also have cycled back into the water column (*36*, *37*), making it available to pelagic or planktonic organisms.

Although these local conditions conspired to make phosphate more bioavailable, they need not correspond to increases in sedimentary phosphate minerals. Phosphate deposits are neither ubiquitous nor the most important products of redox oscillation in modern marine basins (*36*). Instead, major episodes of phosphogenesis, largely postdating the Fifteenmile succession, speak most directly to the interaction between pore water PO_4 and Fe, microbial ecology,

and the concentration of phosphorus at the seafloor in response to pervasive oxidation across continental margins (*38*).

Paleobiological implications

We suggest that the ASMs were inhabitants of a world in transition that facilitated the evolution of HAP biomineralization. Although ASM fossils have thus far only been found at Mount Slipper, it is unlikely that the clade evolved solely within this specific basin; instead, the results presented here suggest that the ASMs represent the evolution of a novel biomineralization capability that may have been confined to a limited temporal window controlled by the availability of essential geochemical building blocks. Although the role of phosphate availability in the relative success and eventual demise of the ASMs is unclear, the phylogenetic distribution of biominerals provides important clues. Phosphate biomineralization is not a major mode of mineralization among Phanerozoic microeukaryotic groups. Although it subsequently appeared in metazoans (brachiopods and chordates), it has only been cursorily identified in one clade of freshwater green algae (*2*, *39*). In contrast, both $CaCO_3$ biomineralization and SiO_2 biomineralization are pervasive across many microeukaryotic clades (*2*). These differences may reflect long-term patterns in the relative abundances of phosphorus versus Ca, CO_3, and SiO_2 in later Neoproterozoic and Phanerozoic seawater (silica is limited in surface waters now because of uptake by diatoms but was likely higher before their evolution) (*40*).

Neoproterozoic tectonic and environmental change may have promoted increased bioavailable phosphate, but what led to the selective pressure on ASMs to biomineralize? The well-documented proliferation of eukaryotes in the early Neoproterozoic (*8*, *24*, *26*) is associated with the evolution or escalation of predation by eukaryotes of other eukaryotes, known as eukaryvory (*8*, *41*, *42*); this in turn would lead to an adaptive advantage for eukaryotic mineralized scale formation (*40*). However, although eukaryvory could be presumed to have imposed a long-term unidirectional drive to skeletonize throughout the Neoproterozoic, the phosphatic ASM taxa and the first metazoan $CaCO_3$ skeletons are separated by roughly 200 million years (*2*). Although primary biomineralized structures are not found in other Neoproterozoic strata until the latest Ediacaran, recalcitrant tests are. Tonian vase-shaped microfossils and Cryogenian agglutinated tests both support the inference that organic or agglutinated armoring offered an advantageous solution in the absence of biomineralization (*26*, *41*, *43*). Thus, our findings indicate that the coincidence of favorable ocean chemistry and the presence of selective pressure via eukaryvory may have shaped the temporal distribution of biomineralized structures in the Neoproterozoic.

These results contribute to an emerging and nuanced picture of early Neoproterozoic tectonic, environmental, and biological change. In the context of existing global geochronological, paleontological, and geochemical data sets, our data leave open the possibility that the proliferation of eukaryotes and the advent of phosphate biomineralization were connected by a fundamental reorganization of the P cycle (*26*, *44*). Although this relationship is speculative on the basis of our current understanding of Tonian biogeochemical cycling, our data do support an increase in bioavailable phosphate during this interval of the Neoproterozoic. Much as today, the ancient P cycle was almost certainly closely linked to those of C, O, S, and Fe via the redox state of the oceans as well as biological nutrient cycling (*10*, *11*, *32*, *36*). Tectonically and/or environmentally driven changes to P cycling may have triggered a cascade of biogeochemical effects that released organisms from nutrient stress, potentially driving competition and evolutionary innovation, including perhaps the rise of eukaryvory. Thus, our results may lead to new ideas about the cause of the phylogenetic radiation of eukaryotic clades and the increased diversity of fossils seen from the Tonian into the Ediacaran (*26*, *44*). Regardless of larger impacts on Neoproterozoic ecosystems, the enhanced bioavailability of P provided a new, if temporally limited, opportunity for eukaryotes to explore biomineralization for what may have been the first time in Earth's history.

MATERIALS AND METHODS

Sedimentology and biostratigraphy

All of the samples were collected in 2009 and 2014 from detailed measured stratigraphic sections near Mount Slipper on the Yukon-Alaska border, which is located at N65°15′55, W140°56′42. These units were previously described as the upper shale and "upper carbonate" of the Upper Tindir Group by Macdonald *et al.* (*7*); this nomenclature was supplanted by correlation with the Fifteenmile Group by Macdonald *et al.* (*34*, *45*). The fossiliferous strata of the Fifteenmile Group consist of approximately 60 m of interbedded planar-laminated lime mudstone, calcareous black and gray shale, and sparse tabular-clast conglomerate (Fig. 1 and fig. S1). ASMs are found in both chert and carbonate throughout approximately 60 m of section (*6*). These strata overlie ~320 m of black and gray shale interbedded with minor intervals of calcareous shale and lime mudstone and massive and channelized quartz arenite, and they are overlain by ~400 m of massive clast-supported dolorudstone, planar-laminated to locally cross-laminated dolograinstone and dolowackestone, and minor calcareous shale and lime mudstone (Fig. 1). The fossiliferous interval also contains minor centimeter-scale carbonate-replaced precipitates that resemble gypsum pseudomorphs (fig. S1D); this is consistent with the increase in disseminated gypsum seen just below the fossiliferous horizon and supports evidence of restriction (Fig. 1). Previous workers considered the fossiliferous deposits to represent subtidal strata in an abrupt shoaling-upward sequence (*4*, *7*, *46*, *47*); however, the abundance of very thin to thin laminae, the absence of wave-generated bedforms, and the presence of matrix-supported debris flow deposits suggest that they were deposited well below storm wave base in a distal slope setting. All of the deepwater strata, as well as the allochthonous debris flow units, contain chert, but the chert is highly variable in abundance, distribution, and form.

High-resolution transmission electron microscopy

For fossil analyses, carbonate hand samples were cleaned, trimmed, and crushed into ca. 1-cm^3 pieces. Crushed rocks were then dissolved using 20% acetic acid for 24 to 48 hours. Macerates were rinsed and filtered through an 11-μm mesh filter. Macerated material was deposited onto a glass slide and air-dried. Fossils were picked individually from dried residues using a Prior Scientific micromanipulator. Picked fossils were placed directly onto 400-mesh copper TEM grids coated with formvar. Fossil specimens were analyzed at the David Cockayne Centre for Electron Microscopy at the University of Oxford using a Jeol JEM-3000F field-emission gun TEM. Images and selected area electron diffraction data were acquired at 200 kV and analyzed using Gatan Digital Micrograph version 3.4. After distance ratios and angles of low-index reflections were measured, selected area electron diffraction data were indexed using data from (*48*). Chemical microanalysis was performed using an Oxford Instruments energy-dispersive x-ray spectrometer (EDS) with a super atmospheric thin window detector. EDS data were

converted to elemental abundances using absorption corrections and thickness in the AZtecTEM software suite.

X-ray diffraction and TEM analyses

Powder x-ray diffraction was performed on bulk sample powders by hand in an agate mortar and pestle. Samples were side-loaded into cavity holders and analyzed using a PANalytical Empyrean Series 2 diffractometer operating at 40 kV and 40 mA with a Co Kα source. Samples were analyzed while continuously rotated, and data were acquired from 5° to 85° 2θ using a step size of 0.026°. Diffraction data were reduced using the HighScore Plus software suite, and mineral identifications were based on correspondence to the International Centre for Diffraction Data Powder Diffraction File 4+ database. In addition, clay mineral speciation and polytype identification were performed by scanning from 69° to 75° 2θ using a step size of 0.026° and count rates of 200 s per step. In this way, mineral-specific 060 reflections were quantified, and clay mineral abundances were expressed as a relative fraction of the total clay content (*49*).

$\delta^{13}C_{carb}$ and $\delta^{18}O_{carb}$ analyses

We present 92 new carbonate carbon ($\delta^{13}C_{carb}$) and oxygen ($\delta^{18}O_{carb}$) isotopic measurements from two stratigraphic sections of the Fifteenmile Group (all data are presented in table S1). Fist-sized to golf ball–sized hand samples were collected at 0.25- to 2-m resolution through measured sections for carbonate carbon and oxygen isotope chemostratigraphy. $\delta^{13}C_{carb}$ and $\delta^{18}O_{carb}$ isotopic results are reported in per mil notation of $^{13}C/^{12}C$ and $^{18}O/^{16}O$, respectively, relative to the standard VPDB (Vienna Pee Dee Belemnite). Carbonate samples were cut perpendicular to bedding and carefully microdilled (~2 to 10 mg of powder) to avoid secondary veins, cements, and siliciclastic components. $\delta^{13}C_{carb}$ and $\delta^{18}O_{carb}$ isotopic data from section J1407 were acquired simultaneously on a VG Optima dual-inlet isotope ratio mass spectrometer coupled with a VG Isocarb preparation device (Micromass) in the Laboratory for Geochemical Oceanography at Harvard University. Approximately 1 mg of sample powder was reacted in a common, purified phosphoric acid (H_3PO_4) bath at 90°C. The evolved CO_2 was collected cryogenically and analyzed using in-house reference gas. Measured data were calibrated to VPDB using the Carrara marble standard (CM2). Total analytical errors (1σ) are better than ±0.1 per mil (‰) for both $\delta^{13}C_{carb}$ and $\delta^{18}O_{carb}$ on the basis of repeat analysis of standards and samples. Increasing the reaction time to 11 min for dolomite samples minimized "memory effects" resulting from the common acid bath system, with the total memory effect estimated at <0.1‰ based on the reproducibility of standards run directly after samples. $\delta^{13}C_{carb}$ and $\delta^{18}O_{carb}$ isotope ratios from section P1401 were measured on a Nu Perspective dual-inlet isotope ratio mass spectrometer connected to a NuCarb carbonate preparation system at the McGill University Stable Isotope Laboratory in Montréal, Canada. Approximately 30 to 100 μg of sample powder was weighed into glass vials and reacted individually with H_3PO_4 after heating to 90°C for 1 hour. The released CO_2 was collected cryogenically, and isotope ratios were measured against in-house reference gas in dual-inlet mode. Samples were calibrated to VPDB using in-house standards. Errors are about 0.05‰ (1σ) for both $\delta^{13}C$ and $\delta^{18}O$.

Re-Os geochronology

For Re-Os analysis, all weathered surfaces were removed with a rock saw with a diamond-edged blade, and samples were then hand-polished using a diamond-encrusted polishing pad to remove cutting marks and eliminate any potential for contamination from the saw blade. The samples (>30 g per sample) were dried overnight at ~60°C and then crushed to a fine (~100 μm) powder in a SPEX 8500 Shatterbox using a zirconium grinding container and puck to homogenize any Re and Os heterogeneity present in the samples (*50*). Wet chemistry procedures for Re and Os isotope analyses were performed following the methods outlined in the studies of Selby and Creaser (*51*) and Kendall *et al.* (*52*) at the Harvard University Hoffman Laboratories. For J1406 samples, between 0.7 and 0.73 g of powder, together with a known amount of a mixed ^{185}Re and ^{190}Os tracer solution (spike), was digested and equilibrated in borosilicate Carius tubes in 10 ml of a $Cr^{VI}O_3$-H_2SO_4 (0.25 g/ml) solution. The Carius tubes were sealed and then heated (50°C per 30-min step heating) to 220°C for 48 hours. Rhenium and osmium were isolated and purified using solvent extraction [NaOH, $(CH_3)_2CO$, and $CHCl_3$], microdistillation, anion column chromatography methods, and negative thermal ionization mass spectrometry, as outlined by Selby and Creaser (*51*) and Cumming *et al.* (*53*). The $Cr^{VI}O_3$-H_2SO_4 digestion method was used because it has been shown to preferentially liberate hydrogenous Re and Os, yielding more accurate and precise age determinations (*51*, *52*, *54*).

The purified Re and Os fractions were loaded onto Ni and Pt filaments, respectively, with the isotopic measurements performed using a Thermo Electron Triton mass spectrometer at the Radiogenic Isotope Geochemistry Laboratory, Department of Earth Sciences, Dartmouth College, via static Faraday collection for Re and ion counting using a secondary electron multiplier in peak-hopping mode for Os. Total procedural blanks during this study were 14.6 ± 0.16 pg and 0.05 ± 0.01 pg (SD, 1σ; $n = 3$) for Re and Os, respectively, with an average $^{187}Os/^{188}Os$ value of 0.61 ± 0.03 ($n = 3$). Uncertainties for $^{187}Re/^{188}Os$ and $^{187}Os/^{188}Os$ were determined by error propagation of uncertainties in Re and Os mass spectrometer measurements, blank abundances and isotopic compositions, spike calibrations, and reproducibility of standard Re and Os isotopic values. The Re-Os isotopic data including the 2σ calculated uncertainties for $^{187}Re/^{188}Os$ and $^{187}Os/^{188}Os$ and the associated error correlation function (rho) were regressed to yield a Re-Os date using Isoplot version 3.7 and the λ ^{187}Re constant of 1.666×10^{-11} per year (*55*, *56*). The age uncertainty including the uncertainty of 0.35% in the ^{187}Re decay constant only affects the third decimal place (*56*, *57*).

To guarantee mass spectrometry reproducibility, two in-house Re (dissolved high-purity Re metal) and Os [Durham Romil Osmium Standard (DROsS)] solution standards were analyzed. The Re solution standard yields an average $^{185}Re/^{187}Re$ ratio of 0.598071 ± 0.001510 (SD, 1; $n = 4$), which is in agreement with the value reported for the AB-1 standard (0.59874 ± 0.00051) (*58*, *59*). The Os isotope reference solution (DROsS) gave an $^{187}Os/^{188}Os$ ratio of 0.160891 ± 0.000559 (SD, 1; $n = 6$), which is in agreement with previous studies (*58*, *59*) (and references therein).

Elemental Re and Os abundances for samples J1406 range from 3.4 to 20.9 ng/g and 171 to 1236 pg/g, respectively, with $^{187}Re/^{188}Os$ and $^{187}Os/^{188}Os$ values ranging from 30 to 117 and 0.845 to 2.017, respectively (see the Supplementary Materials). Regression of the isotope data for samples J1406 yields a model 1 age of 810.7 ± 5.8 (6.3) Ma (bracketed age uncertainty includes the 0.35% uncertainty in the ^{187}Re decay constant; $n = 8$; MSWD, 0.47; 2σ uncertainties; initial $^{187}Os/^{188}Os = 0.43 \pm 0.01$).

SUPPLEMENTARY MATERIALS

Supplementary material for this article is available at http://advances.sciencemag.org/cgi/content/full/3/6/e1700095/DC1

fig. S1. Stratigraphy and sedimentology at Mount Slipper.

fig. S2. Additional TEM and HR-TEM images of an ASM specimen.
fig. S3. Energy-dispersive x-ray spectrograph of an ASM sample.
fig. S4. Additional geochemical and mineralogical data for Mount Slipper.
table S1. All geochemical and geochronological data presented in the paper.

REFERENCES AND NOTES

1. R. M. Hazen, D. Papineau, W. Bleeker, R. T. Downs, J. M. Ferry, T. J. McCoy, D. A. Sverjensky, H. Yang, Mineral evolution. *Am. Mineral.* **93**, 1693–1720 (2008).
2. A. H. Knoll, Biomineralization and evolutionary history. *Rev. Mineral. Geochem.* **54**, 329–356 (2003).
3. S. Weiner, P. M. Dove, An overview of biomineralization processes and the problem of the vital effect. *Rev. Mineral. Geochem.* **54**, 1–29 (2003).
4. C. W. Allison, J. W. Hilgert, Scale microfossils from the early Cambrian of northwest Canada. *J. Paleo.* **60**, 973–1015 (1986).
5. P. A. Cohen, J. W. Schopf, N. J. Butterfield, A. B. Kudryavtsev, F. A. Macdonald, Phosphate biomineralization in mid-Neoproterozoic protists. *Geophys. J. R. Astron. Soc.* **39**, 539–542 (2011).
6. P. A. Cohen, A. H. Knoll, Scale microfossils from the mid-Neoproterozoic Fifteenmile Group, Yukon Territory. *J. Paleo.* **86**, 775–800 (2012).
7. F. A. Macdonald, P. A. Cohen, F. Dudás, D. P. Schrag, Early Neoproterozoic scale microfossils in the Lower Tindir Group of Alaska and the Yukon Territory. *Geophys. J. R. Astron. Soc.* **38**, 143–146 (2010).
8. A. H. Knoll, Paleobiological perspectives on early eukaryotic evolution. *Cold Spring Harb. Perspect. Biol.* **6**, a016121 (2014).
9. M. E. Katz, Z. V. Finkel, D. Grzebyk, A. H. Knoll, P. G. Falkowski, Evolutionary trajectories and biogeochemical impacts of marine eukaryotic phytoplankton. *Annu. Rev. Ecol. Evol. Syst.* **35**, 523–556 (2004).
10. A. Paytan, K. McLaughlin, The oceanic phosphorus cycle. *Chem. Rev.* **107**, 563–576 (2007).
11. C. R. Benitez-Nelson, The biogeochemical cycling of phosphorus in marine systems. *Earth Sci. Rev.* **51**, 109–135 (2000).
12. T. F. Thingstad, M. D. Krom, R. F. C. Mantoura, G. A. F. Flaten, S. Groom, B. Herut, N. Kress, C. S. Law, A. Pasternak, P. Pitta, S. Psarra, F. Rassoulzadegan, T. Tanaka, A. Tselepides, P. Wassmann, E. M. S. Woodward, C. W. Riser, G. Zodiatis, T. Zohary, Nature of phosphorus limitation in the ultraoligotrophic Eastern Mediterranean. *Science* **309**, 1068–1071 (2005).
13. J. Rakovan, Growth and surface properties of apatite. *Rev. Mineral. Geochem.* **48**, 51–86 (2002).
14. L. Wang, G. H. Nancollas, Calcium orthophosphates: Crystallization and dissolution. *Chem. Rev.* **108**, 4628–4669 (2008).
15. A. Navrotsky, Energetic clues to pathways to biomineralization: Precursors, clusters, and nanoparticles. *Proc. Natl. Acad. Sci. U.S.A.* **101**, 12096–12101 (2004).
16. F. A. Macdonald, M. D. Schmitz, J. L. Crowley, C. F. Roots, D. S. Jones, A. C. Maloof, J. V. Strauss, P. A. Cohen, D. T. Johnston, D. P. Schrag, Calibrating the Cryogenian. *Science* **327**, 1241–1243 (2010).
17. N. L. Swanson-Hysell, A. C. Maloof, D. J. Condon, G. R. T. Jenkin, M. Alene, M. M. Tremblay, T. Tesema, A. D. Rooney, B. Haileab, Stratigraphy and geochronology of the Tambien Group, Ethiopia: Evidence for globally synchronous carbon isotope change in the Neoproterozoic. *Geology* **43**, 323–326 (2015).
18. E. A. Sperling, G. P. Halverson, A. H. Knoll, F. A. Macdonald, D. T. Johnston, A basin redox transect at the dawn of animal life. *Earth Planet. Sci. Lett.* **371–372**, 143–155 (2013).
19. G. M. Cox, G. P. Halverson, R. K. Stevenson, M. Vokaty, A. Poirier, M. Kunzmann, Z.-X. Li, S. W. Denyszyn, J. V. Strauss, F. A. Macdonald, Continental flood basalt weathering as a trigger for Neoproterozoic Snowball Earth. *Earth Planet. Sci. Lett.* **446**, 89–99 (2016).
20. J. L. Banner, G. N. Hanson, Calculation of simultaneous isotopic and trace element variations during water-rock interaction with applications to carbonate diagenesis. *Geochim. Cosmochim. Acta* **54**, 3123–3137 (1990).
21. G. P. Halverson, A. C. Maloof, D. P. Schrag, F. Dudás, M. Hurtgen, Stratigraphy and geochemistry of a ca 800 Ma negative carbon isotope interval in northeastern Svalbard. *Chem. Geol.* **237**, 5–27 (2007).
22. A. D. Rooney, J. V. Strauss, A. D. Brandon, F. A. Macdonald, A Cryogenian chronology: Two long-lasting synchronous Neoproterozoic glaciations. *Geophys. J. R. Astron. Soc.* **43**, 459–462 (2015).
23. A. D. Rooney, F. A. Macdonald, J. V. Strauss, F. Dudás, C. Hallmann, D. Selby, Re-Os geochronology and coupled Os-Sr isotope constraints on the Sturtian snowball Earth. *Proc. Natl. Acad. Sci. U.S.A.* **111**, 51–56 (2014).
24. J. V. Strauss, A. D. Rooney, F. A. Macdonald, A. D. Brandon, A. H. Knoll, 740 Ma vase-shaped microfossils from Yukon, Canada: Implications for Neoproterozoic chronology and biostratigraphy. *Geology* **42**, 659–662 (2014).
25. J. P. Pu, S. A. Bowring, J. Ramezani, P. Myrow, T. D. Raub, E. Landing, A. Mills, E. Hodgin, F. A. Macdonald, Dodging snowballs: Geochronology of the Gaskiers glaciation and the first appearance of the Ediacaran biota. *Geophys. J. R. Astron. Soc.* **44**, 955–958 (2016).
26. P. A. Cohen, F. A. Macdonald, The Proterozoic record of eukaryotes. *Paleobiology* **41**, 610–632 (2015).
27. A. H. Knoll, E. J. Javaux, D. Hewitt, P. Cohen, Eukaryotic organisms in Proterozoic oceans. *Philos. Trans. R. Soc. B* **361**, 1023–1038 (2006).
28. D. H. Erwin, M. Laflamme, S. M. Tweedt, E. A. Sperling, D. Pisani, K. J. Peterson, The Cambrian conundrum: Early divergence and later ecological success in the early history of animals. *Science* **334**, 1091–1097 (2011).
29. E. C. Turner, A. Bekker, Thick sulfate evaporite accumulations marking a mid-Neoproterozoic oxygenation event (Ten Stone Formation, Northwest Territories, Canada). *Geol. Soc. Am. Bull.* **128**, 203–222 (2015).
30. E. A. Sperling, C. J. Wolock, A. S. Morgan, B. C. Gill, M. Kunzmann, G. P. Halverson, F. A. Macdonald, A. H. Knoll, D. T. Johnston, Statistical analysis of iron geochemical data suggests limited late Proterozoic oxygenation. *Nature* **523**, 451–454 (2015).
31. N. J. Planavsky, C. T. Reinhard, X. Wang, D. Thomson, P. McGoldrick, R. H. Rainbird, T. Johnson, W. W. Fischer, T. W. Lyons, Low mid-Proterozoic atmospheric oxygen levels and the delayed rise of animals. *Science* **346**, 635–638 (2014).
32. C. T. Reinhard, N. J. Planavsky, B. C. Gill, K. Ozaki, L. J. Robbins, T. W. Lyons, W. W. Fischer, C. Wang, D. B. Cole, K. O. Konhauser, Evolution of the global phosphorus cycle. *Nature* **541**, 386–389 (2017).
33. F. Horton, Did phosphorus derived from the weathering of large igneous provinces fertilize the Neoproterozoic ocean? *Geochem. Geophys. Geosyst.* **16**, 1723–1738 (2015).
34. F. A. Macdonald, G. P. Halverson, J. V. Strauss, E. F. Smith, G. Cox, E. A. Sperling, C. F. Roots, Early Neoproterozoic Basin Formation in Yukon, Canada: Implications for the make-up and break-up of Rodinia. *Geosci. Can.* **39**, 77–99 (2012).
35. G. W. O'Brien, A. R. Milnes, H. H. Veeh, D. T. Heggie, S. R. Riggs, D. J. Cullen, J. F. Marshall, P. J. Cook, Sedimentation dynamics and redox iron-cycling: Controlling factors for the apatite–glauconite association on the East Australian continental margin. *Geol. Soc. London Spec. Publ.* **52**, 61–86 (1990).
36. H. P. Mort, C. P. Slomp, B. G. Gustafsson, T. J. Andersen, Phosphorus recycling and burial in Baltic Sea sediments with contrasting redox conditions. *Geochim. Cosmochim. Acta* **74**, 1350–1362 (2010).
37. D. J. Conley, C. Humborg, L. Rahm, O. P. Savchuk, F. Wulff, Hypoxia in the Baltic sea and basin-scale changes in phosphorus biogeochemistry. *Environ. Sci. Technol.* **36**, 5315–5320 (2002).
38. P. K. Pufahl, Bioelemental sediments, in *Facies Models* (Geological Association of Canada, ed. 4, 2010), pp. 477–503.
39. D. S. Domozych, B. Wells, P. J. Shaw, Basket scales of the green alga, *Mesostigma viride*: Chemistry and ultrastructure. *J. Cell Sci.* **100**, 397–407 (1991).
40. A. H. Knoll, B. Kotrc, in *Protistan Skeletons: A Geologic History of Evolution and Constraint* (Springer, 2015), pp. 1–16.
41. S. Porter, The rise of predators. *Geophys. J. R. Astron. Soc.* **39**, 607–608 (2011).
42. S. M. Porter, Tiny vampires in ancient seas: Evidence for predation via perforation in fossils from the 780–740 million-year-old Chuar Group, Grand Canyon, USA. *Proc. Biol. Sci.* **283**, 20160221 (2016).
43. T. Bosak, D. J. G. Lahr, S. B. Pruss, F. A. Macdonald, L. Dalton, E. Matys, Agglutinated tests in post-Sturtian cap carbonates of Namibia and Mongolia. *Earth Planet. Sci. Lett.* **308**, 29–40 (2011).
44. L. W. Parfrey, D. J. G. Lahr, A. H. Knoll, L. A. Katz, Estimating the timing of early eukaryotic diversification with multigene molecular clocks. *Proc. Natl. Acad. Sci. U.S.A.* **108**, 13624–13629 (2011).
45. F. A. Macdonald, E. F. Smith, J. V. Strauss, G. M. Cox, G. P. Halverson, C. F. Roots, Neoproterozoic and early Paleozoic correlations in the western Ogilvie Mountains, Yukon. *Yukon Explor. Geol.* **2010**, 161–182 (2010).
46. F. A. Macdonald, P. A. Cohen, The Tatonduk inlier, Alaska–Yukon border. *Geol. Soc. London Memoirs* **36**, 389–396 (2011).
47. C. W. Allison, Siliceous microfossils from the Lower Cambrian of northwest Canada: Possible source for biogenic chert. *Science* **211**, 53–55 (1981).
48. R. M. Wilson, J. C. Elliott, S. E. P. Dowker, Rietveld refinement of the crystallographic structure of human dental enamel apatites. *Am. Mineral.* **84**, 1406–1414 (1999).
49. J. Środoń, V. A. Drits, D. K. McCarty, J. C. C. Hsieh, D. D. Eberl, Quantitative x-ray diffraction analysis of clay-bearing rocks from random preparations. *Clays Clay Miner.* **49**, 514–528 (2001).
50. B. Kendall, R. A. Creaser, D. Selby, ^{187}Re-^{187}Os geochronology of Precambrian organic-rich sedimentary rocks. *Geol. Soc. London Spec. Publ.* **326**, 85–107 (2009).
51. D. Selby, R. A. Creaser, Re–Os geochronology of organic rich sediments: An evaluation of organic matter analysis methods. *Chem. Geol.* **200**, 225–240 (2003).
52. B. S. Kendall, R. A. Creaser, G. M. Ross, D. Selby, Constraints on the timing of Marinoan "Snowball Earth" glaciation by 187 Re–187 Os dating of a Neoproterozoic, post-glacial black shale in Western Canada. *Earth Planet. Sci. Lett.* **222**, 729–740 (2004).
53. V. M. Cumming, S. W. Poulton, A. D. Rooney, D. Selby, Anoxia in the terrestrial environment during the late Mesoproterozoic. *Geophys. J. R. Astron. Soc.* **41**, 583–586 (2013).

54. A. D. Rooney, D. M. Chew, D. Selby, Re–Os geochronology of the Neoproterozoic–Cambrian Dalradian Supergroup of Scotland and Ireland: Implications for Neoproterozoic stratigraphy, glaciations and Re–Os systematics. *Precambrian Res.* **185**, 202–214 (2011).
55. K. Ludwig, Isoplot/Ex, Version 3.7: A Geochronological Toolkit for Microsoft Excel (Special Publication 5, Berkeley Geochronology Center, 2008), 75 p.
56. M. I. Smoliar, R. J. Walker, J. W. Morgan, Re-Os ages of group IIA, IIIA, IVA, and IVB iron meteorites. *Science* **271**, 1099–1102 (1996).
57. D. Selby, R. A. Creaser, H. J. Stein, R. J. Markey, J. L. Hannah, Assessment of the ^{187}Re decay constant by cross calibration of Re–Os molybdenite and U–Pb zircon chronometers in magmatic ore systems. *Geochim. Cosmochim. Acta* **71**, 1999–2013 (2007).
58. A. J. Finlay, D. Selby, D. R. Gröcke, Tracking the Hirnantian glaciation using Os isotopes. *Earth Planet. Sci. Lett.* **293**, 339–348 (2010).
59. A. D. Rooney, D. Selby, J.-P. Houzay, P. R. Renne, Re–Os geochronology of a Mesoproterozoic sedimentary succession, Taoudeni basin, Mauritania: Implications for basin-wide correlations and Re–Os organic-rich sediments systematics. *Earth Planet. Sci. Lett.* **289**, 486–496 (2010).

Acknowledgments: This project was inspired by the work of S. Bowring, whose enthusiasm and dedication for providing high-precision age constraints on key evolutionary episodes in Earth's history of life are truly unparalleled. We thank D. Schrag for use of the Laboratory for Geochemical Oceanography at Harvard University and G. Halverson for use of the Stable Isotope Laboratory at McGill University. F. A. Macdonald, D. Selby, and J. F. Taylor provided logistical and analytical support. L. Stamp and L. Nelson aided in the field. N. Piatzyc and K. Jurkschat provided technical support. **Funding:** We thank the NASA Astrobiology Institute MIT (Massachusetts Institute of Technology) node, Dartmouth College, Williams College, and the Leverhulme Trust for financial support. A.D.R. was supported by a NASA Astrobiology Postdoctoral Fellowship. M.S. acknowledges funding from Dartmouth College. **Author contributions:** P.A.C. and J.V.S. designed the study. P.A.C. and J.V.S. performed fieldwork. P.A.C. and N.T. performed microscopic analyses. N.T. performed mineralogical analyses. A.D.R. and M.S. performed geochronological analyses. P.A.C., J.V.S., and N.T. wrote the paper with help from A.D.R. and M.S. **Competing interests:** The authors declare that they have no competing interests. **Data and materials availability:** All data needed to evaluate the conclusions in the paper are present in the paper and/or the Supplementary Materials. Additional data related to this paper may be requested from the authors.

Submitted 9 January 2017
Accepted 1 June 2017
Published 28 June 2017
10.1126/sciadv.1700095

Citation: P. A. Cohen, J. V. Strauss, A. D. Rooney, M. Sharma, N. Tosca, Controlled hydroxyapatite biomineralization in an ~810 million-year-old unicellular eukaryote. *Sci. Adv.* **3**, e1700095 (2017).